NeuroImage 185 (2019) 198–207

Contents lists available at ScienceDirect

NeuroImage

journal homepage: www.elsevier.com/locate/neuroimage

Rapid solution of the Bloch-Torrey equation in anisotropic tissue: Application to dynamic susceptibility contrast MRI of cerebral white matter

Jonathan Doucette [a,b,*], Luxi Wei [a,c], Enedino Hernández-Torres [a,d], Christian Kames [a,b], Nils D. Forkert [e], Rasmus Aamand [f], Torben E. Lund [f], Brian Hansen [f], Alexander Rauscher [a,b,d]

[a] UBC MRI Research Centre, University of British Columbia, 2221, Wesbrook Mall, Vancouver, BC, Canada
[b] Department of Physics and Astronomy, University of British Columbia, 6224, Agricultural Road, Hennings Building, Room 325, Vancouver, BC, Canada
[c] Department of Medical Biophysics, University of Toronto, Toronto, ON, Canada
[d] Department of Pediatrics, University of British Columbia Faculty of Medicine, Rm 2D19, 4480, Oak Street, BC Children's Hospital, Vancouver, BC, Canada
[e] Department of Radiology and Hotchkiss Brain Institute, University of Calgary, Calgary, AB, Canada
[f] Center of Functionally Integrative Neuroscience (CFIN) and MINDLab, Department of Clinical Medicine, Aarhus University Hospital, Nørrebrogade 44, Building 10G, 5th floor, 8000, Aarhus C, Denmark

ARTICLE INFO

Keywords:
Cerebral blood volume
Cerebral blood flow
Brain perfusion
Functional MRI
Tissue anisotropy
Bloch-torrey equation
Diffusion

ABSTRACT

Blood vessel related magnetic resonance imaging (MRI) contrast provides a window into the brain's metabolism and function. Here, we show that the spin echo dynamic susceptibility contrast (DSC) MRI signal of the brain's white matter (WM) strongly depends on the angle between WM tracts and the main magnetic field. The apparent cerebral blood flow and volume are 20% larger in fibres perpendicular to the main magnetic field compared to parallel fibres. We present a rapid numerical framework for the solution of the Bloch-Torrey equation that allows us to explore the isotropic and anisotropic components of the vascular tree. By fitting the simulated spin echo DSC signal to the measured data, we show that half of the WM vascular volume is comprised of vessels running in parallel with WM fibre tracts. The WM blood volume corresponding to the best fit to the experimental data was 2.82%, which is close to the PET gold standard of 2.6%.

1. Introduction

The distribution of blood in the human brain is regulated via a specialized vascular network. Although the brain comprises only 2% of the total body mass, it receives 15% of the cardiac output (Bouma and Muizelaar, 1990). Cerebral blood flow (CBF), volume (CBV), and oxygenation are, thus, essential parameters of brain physiology and stable levels are required to maintain brain function. MRI is able to probe these parameters, usually via changes in the magnetic properties of the vascular system, to which the MRI signal is exquisitely sensitive. In DSC MRI, a paramagnetic contrast agent (CA) is administered intravenously during the repeated acquisition of a rapid imaging technique (Østergaard et al., 1996b, 1996a), typically gradient echo or a spin echo echo planar imaging (EPI). The contrast mechanism of DSC is a change in coherence due to the field inhomogeneities around the blood vessels. With increasing CA concentration, the vessels become more paramagnetic and the field inhomogeneities become stronger (Ogawa et al., 1990), which results in an accelerated loss of coherence. Analysis of DSC scans usually assumes that the vascular architecture within the voxel is spatially isotropic, and therefore that the local orientation of the vascular tree relative to the main magnetic field plays no role. However, the vascular bed is not isotropic, particularly in white matter. Postmortem images show many vessels running in parallel with WM tracts (Nonaka et al., 2003a, 2003b; Okudera et al., 1999). Microscopic images of a rodent model of ischemia (Cavaglia et al., 2001), and maps of perivascular spaces in humans (Cai et al., 2015) exhibit anisotropy of the vascular architecture. In venography based on susceptibility weighted imaging (SWI) (Deistung et al., 2008; Denk and Rauscher, 2010; Reichenbach and Haacke, 2001), the anisotropy of the vascular system can be readily appreciated in vivo. Furthermore, it has been recently shown that the gradient echo perfusion signal and the maps of CBF and CBV derived therefrom exhibit a strong dependence on the local orientation of WM fibre tracts (Hernández-Torres et al., 2017). Numerical simulations of static spin dephasing that best fit the measured data suggested that about half the blood volume is within larger anisotropic vessels. Gradient echo scans are usually used for DSC experiments, due to their high sensitivity

* Corresponding author. UBC MRI Research Centre, M10 Purdy Pavilion, 2221 Wesbrook Mall, Vancouver, BC, V6T 2B5, Canada
E-mail address: jdoucette@phas.ubc.ca (J. Doucette).

https://doi.org/10.1016/j.neuroimage.2018.10.035
Received 22 June 2018; Received in revised form 9 October 2018; Accepted 11 October 2018
Available online 15 October 2018

to changes in blood oxygenation or CA concentration. However, spin echo scans are also sensitive to the presence of an intravascular CA due to spins losing coherence while diffusing in the magnetically inhomogeneous environment created by the blood vessels (Boxerman et al., 1995).

Since smaller vessels produce shorter ranged field inhomogeneities, loss of coherence due to diffusion is stronger in the vicinity of small vessels, and therefore the spin echo signal is more sensitive to small vessels than to large vessels. For this reason, fMRI, which uses changes in blood oxygenation as an intrinsic contrast mechanism, is more specific to the location and spatial extent of neural activation when acquired with spin echo EPI (Norris, 2012; Uludağ et al., 2009; Uludağ and Blinder, 2018). With anisotropic vascular architecture, the loss of coherence should depend on tissue orientation and give rise to orientation effects. The anisotropy of the cerebral vasculature, in particular in WM, raises several questions: How strongly does the DSC signal depend on the orientation of WM? How much blood resides in the isotropic and anisotropic compartments of the vascular network, and what is the role of vessel size? Based on our previous findings for gradient echo DSC and on the above considerations, we hypothesize that spin echo DSC exhibits tissue orientation effects. In this work, we investigate the vascular architecture experimentally by combining spin echo DSC with diffusion tensor imaging for the analysis of WM fibre orientation. We then fit a model of the spin echo signal for fibre orientations between 0° and 90° from which we extract isotropic and anisotropic components of the vascular tree. These calculations require the solution of the Bloch-Torrey equation, which describes the spin echo signal in a magnetically inhomogeneous environment. Since we fit for the vascular parameters of the orientation dependent DSC signal, thousands of solutions of the Bloch-Torrey equation need to be computed on a large 3D grid that contains an anisotropic vascular tree. To do so in a computationally feasible manner, we developed a framework that is based on the equivalence of the Bloch-Torrey equation to the single-particle time dependent Schrödinger equation.

2. Materials and methods

2.1. Theoretical considerations

We first develop a numerical framework for the investigation of the effect of field inhomogeneities on the DSC signal. The simulation contains a small number of free parameters, which will be determined by fitting the simulated DSC signal data to the corresponding experimental data in a non-linear least squares fashion. The simulated DSC data is the change in transverse relaxation ΔR_2 that occurs due to the administration of the paramagnetic CA. This change in R_2 can be computed by simulating the magnetization within a single WM voxel until an echo time TE, both with and without CA. The resulting ΔR_2 is given by

$$\Delta R_2 = -\frac{1}{\mathrm{TE}}\ln\left(\frac{S}{S_0}\right), \tag{1}$$

where S_0 is the signal before the arrival of the CA, and S is the signal at the time point corresponding to a particular CA concentration (Østergaard et al., 1996b, 1996a). In order to investigate the effect of WM fibre tract orientation on the resulting ΔR_2 values, we define α to be the angle between the main magnetic field and the WM fibre and allow α to vary between 0° and 90° in the simulations. The two major components of the simulations are the generation of the geometry of the problem for a given set of simulation parameters, and the subsequent propagation of the magnetization through time.

The simulation takes place inside a single voxel of dimensions $3 \times 3 \times 3\,\mathrm{mm}^3$, wherein we place an isotropic vascular bed consisting of small blood vessels (with radii in the order of 10 μm), as well as anisotropic vasculature consisting of a variable number L of large blood vessels (with radii in the order of 100 μm) running in parallel with the z-axis surrounded by a fluid-filled perivascular space (Kwee and Kwee, 2007). An example of this geometry with L = 5 anisotropic vessels is shown in Fig. 1. The orientation of the WM fibres is assumed to be parallel to the anisotropic blood vessels, and therefore the WM fibre is oriented in the z-direction as well. The total amount of vasculature contained in the voxel is determined by the blood volume fraction (BVF), a free parameter. The isotropic vasculature is simulated as cylinders with uniformly random orientation and position within the voxel, with radii of 7.0 μm (Meier-Ruge et al., 1980). The total number of isotropic vessels is determined by a second free parameter, the isotropic relative blood volume fraction (iRBVF). The anisotropic vasculature is simulated as uniformly spaced cylinders with axes parallel to the z-axis. The radii of the anisotropic vessels are determined by the anisotropic relative blood volume fraction (aRBVF), a constrained parameter given by aRBVF = 1 − iRBVF.

The voxel may now be thought of as being separated into three regions: vasculature, perivascular space, and the surrounding tissue. In these regions, we prescribe different values for the relaxation rate R_2 and for the magnetic susceptibility χ. The T_2 value of the tissue is set to 69 ms (Stanisz et al., 2005); the T_2 value of the perivascular space is set to the T_2 of CSF at 3T, 1790 ms (Spijkerman et al., 2018); the radius of the perivascular space is chosen to be twice that of the corresponding anisotropic vessel radius (Kwee and Kwee, 2007). Additionally, the value of both R_2 and χ within the blood depends on the peak CA concentration (CA_{PEAK}), the third free parameter of the simulation. The dependence of R_2 and χ on CA_{PEAK} is detailed in our previous study; see equation (4) in (Hernández-Torres et al., 2017). Since χ is non-constant within the voxel, local magnetic field inhomogeneities are induced according to

$$\frac{\delta B(\mathbf{r})}{B_0} = G_\alpha(\mathbf{r}) * \delta\chi(\mathbf{r}), \tag{2}$$

where G_α is the unit dipole kernel defined as

$$G_\alpha(\mathbf{r}) = \frac{1}{4\pi}\frac{3\cos^2(\theta) - 1}{r^3}. \tag{3}$$

This is the forward field calculation for the magnetic field by convolution of the spatial magnetic susceptibility distribution with a unit dipole (Marques and Bowtell, 2008). The spherical radial distance and polar angle (r, θ) in equation (3) are relative to the main magnetic field direction. In our simulations, it is convenient to work in coordinates where the WM fibre is in the z-direction, hence the subscript α on the dipole kernel. The resulting local resonance frequency shift as seen by the diffusing protons is given by

$$\delta\omega(\mathbf{r}) = \gamma \cdot \delta B(\mathbf{r}) \tag{4}$$

In the experimental data, α was computed by taking the angle between the main magnetic field direction and the principal diffusion direction as measured with DTI. Each WM voxel was then sorted into bins according to their α-value. The bin widths were taken to be 5°, resulting in 18 bins corresponding to angles from 2.5° to 87.5° in 5° increments. In the numerical simulations, α varies over these 18 angles in order to match the experimental data. Cross sections of δω in the xy-plane for three different angles α are shown in Fig. 1. Next, we consider the propagation of the magnetization through time, which is described by the Bloch-Torrey equation (Torrey, 1956)

$$\frac{\partial \mathcal{M}}{\partial t} = \gamma\mathcal{M} \times \mathbf{B} - \left[\frac{\mathcal{M}_x}{T_2}, \frac{\mathcal{M}_y}{T_2}, \frac{\mathcal{M}_z - \mathcal{M}_0}{T_1}\right]^{\mathrm{T}} + \nabla \cdot \mathbf{D}\nabla\mathcal{M}. \tag{5}$$

Accounting for diffusion in the presence of the α-dependent field inhomogeneities introduces α-dependent simulated ΔR_2 values. Since $\mathrm{TE} \approx T_2 \ll T_1$, we neglect T_1 effects. We assume isotropic diffusion by setting $\mathbf{D} = D\mathbf{I}$. Additionally, we denote

$$\mathrm{M}: = \mathcal{M}_x + i\mathcal{M}_y \tag{6}$$

the complex transverse magnetization and

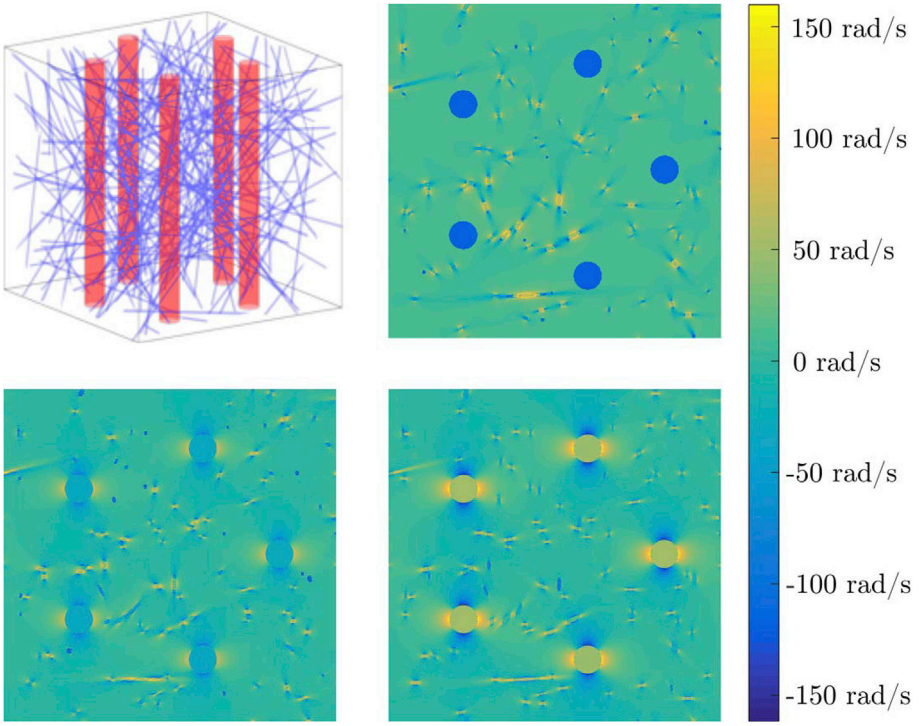

Fig. 1. The top-left figure shows an example voxel geometry. The $3 \times 3 \times 3\,\mathrm{mm}^3$ voxel is populated with an isotropic vascular bed and $L = 5$ anisotropic large vessels in the z-direction. The total volume occupied by the blood vessels is determined by the blood volume fraction BVF. The relative fraction of blood contained in the isotropic vascular bed is determined by the isotropic relative blood volume fraction iRBVF, and the amount of blood contained in the anisotropic vessels is then aRBVF = 1 − iRBVF. The magnetic field generated by this configuration is computed by the convolution of the susceptibility map with the unit dipole kernel. Example cross-sections of the frequency shift map δω are shown for $\alpha = 0°$ (top right), 45° (bottom left), and 90° (bottom right). It can be easily observed that near large vessels, the resonance frequency (i.e. the magnetic field) remains locally relatively constant compared to the resonance frequency near small vessels, which changes rapidly over short distances. Note also the increase in strength and range of inhomogeneities around the large anisotropic vessels as α increases, introducing the dependence on the angle α into the simulations.

$$\Gamma(\mathbf{r}) := R_2(\mathbf{r}) + i\omega(\mathbf{r}) \tag{7}$$

the complex decay rate, where $\omega(\mathbf{r}) = \omega_0 + \delta\omega(\mathbf{r})$ with $\omega_0 = \gamma B_0$, and $R_2(\mathbf{r})$ is the piecewise constant R_2 value taking different values in tissue and in blood. The resulting Bloch-Torrey equation is

$$\frac{\partial}{\partial t} M(\mathbf{r}, t) = D\nabla^2 M(\mathbf{r}, t) - \Gamma(\mathbf{r}) M(\mathbf{r}, t), \tag{8}$$

where ∇^2 is the 3D Laplacian operator. The Bloch-Torrey equation admits no closed form for general $\Gamma(\mathbf{r})$, and must be solved numerically.

At this point, we change coordinates such that the WM fibre is in the z-direction and so M represents the magnetization transverse to the magnetic field $\mathbf{B} = B_0\,[\sin\alpha,\ 0,\ \cos\alpha]^T$. This is purely a matter of convenience, as now instead of generating new vasculature networks for each desired WM fibre angle α, the WM fibres can remain fixed and only the frequency shifts $\delta\omega(\mathbf{r})$ must be recomputed.

The simulation contains four free parameters: the peak contrast agent concentration CA_{PEAK}, the total blood volume fraction BVF, the isotropic relative blood volume fraction iRBVF, and the total number of large anisotropic vessels L. The task is now to find parameters such that the solutions to equation (8) result in a ΔR_2 vs. α curve that is as close as possible to the experimental ΔR_2 vs. α data. The basic algorithm to do so is as follows: for a given number of anisotropic vessels L choose an initial set of parameters CA_{PEAK}, BVF, and iRBVF; for each angle α calculate the corresponding 3D map of resonance frequencies and initialize the magnetization with the constant value of $M(\mathbf{r}, 0) = i = \sqrt{(-1)}$; propagate the magnetization by solving the Bloch-Torrey equation both with and without CA for each angle α to obtain a simulated ΔR_2 vs. α curve; compare the resulting curve with the observed ΔR_2 vs. α data set; choose new parameters based on an error minimization algorithm such as gradient descent; repeat until convergence of parameters. Approximately 25–30 iterations are needed for convergence of a typical set of parameters to a tolerance on the order of 0.1% given an appropriate initial guess. Due to the fact that the Bloch-Torrey equation must be solved both with and without CA for each of the 18 angles α, approximately 1000 solutions to the Bloch-Torrey equation must be computed for a given initial guess. For this reason, and because the anisotropic nature of the vascular tree requires a simulation in three dimensions, rapid computation is required.

2.2. Fast solution of the Bloch-Torrey equation

In order to solve equation (8) efficiently, we begin by considering techniques used to solve the imaginary-time Schrödinger equation (Wick, 1954), which is equivalent to the Bloch-Torrey equation (8) (Ziener et al., 2009, 2012). In this analogy, $-D\nabla^2$ is the kinetic energy operator K, and Γ is the complex potential energy operator V. Note that Γ is formally distinct from $\Gamma(\mathbf{r})$: Γ is the operator whose action on a function is to multiply pointwise by $\Gamma(\mathbf{r})$, just as ∇^2 is the operator whose action is to apply the Laplacian.

This approach allows us to use *Diffusion Monte Carlo* (DMC) techniques for solving the Bloch-Torrey equation (8). DMC methods were originally developed to solve the imaginary-time Schrödinger equation by approximating the evolution operator $\exp(-\hat{H}t)$ which acts on an initial wave function $\Psi(\mathbf{r}, t = 0)$, where $\hat{H}$ is the Hamiltonian of the system. In our case, $\hat{H} = K + V = -D\nabla^2 + \Gamma$ and $\Psi(\mathbf{r}, 0) = M(\mathbf{r}, 0)$. We use a particular set of DMC methods known as *splitting methods*, wherein the evolution operator of the imaginary-time Schrödinger equation is approximated by decoupling the actions of the kinetic and potential energy terms over sufficiently small time intervals Δt. We have the approximations (Bader et al., 2013; Guardiola, 1998)

$$e^{-\hat{H}\Delta t} = e^{-(K+V)\Delta t} \tag{9}$$

$$e^{-\hat{H}\Delta t} = e^{-K\Delta t} e^{-V\Delta t} + \mathcal{O}\left(\Delta t^2\right) \tag{10}$$

$$e^{-\hat{H}\Delta t} = e^{-V\Delta t/2} e^{-K\Delta t} e^{-V\Delta t/2} + \mathcal{O}\left(\Delta t^3\right). \tag{11}$$

Equations (10) and (11) hold for any pair of linear operators K and V in the limit of small Δt. The error terms occur due to the fact that in general, K and V do not commute. Otherwise, these approximations would both be exact. Additionally, hermiticity of the Hamiltonian is not required, as would typically be the case in quantum mechanics.

Importantly, in our case the actions of the evolution operators e^{-Kt} and e^{-Vt} in approximations 10 and 11 have the known closed forms

(Guardiola, 1998)

$$e^{-Kt}\mathrm{M}(\mathbf{r},0) = \Phi(\mathbf{r},t) * \mathrm{M}(\mathbf{r},0) \tag{12}$$

$$e^{-Vt}\mathrm{M}(\mathbf{r},0) = e^{-\Gamma(\mathbf{r})t}\mathrm{M}(\mathbf{r},0), \tag{13}$$

where Φ(**r**, t) is the Gaussian kernel defined as

$$\Phi(\mathbf{r},t) := \frac{1}{(4\pi Dt)^{3/2}} e^{-\mathrm{r}^2/4Dt} \tag{14}$$

and * denotes the convolution over space. Note that, as opposed to using equation (9) which does not in general admit a closed form, the evolution of the initial transverse magnetization M(**r**, 0) via equation (12) or 13 is extremely fast to compute. Equation (12) simply convolves the initial state with a Gaussian kernel (or equivalently, it applies uniform smoothing of width $\sigma = \sqrt{2Dt}$). This convolution can be computed efficiently using the Fast Fourier Transform (FFT), since the boundary conditions are taken to be periodic (Nguyen et al., 2014). Equation (13) involves point-wise multiplication and exponentiation, and thus is even faster to compute.

The approximate solutions given by equations (10) and (11) can be interpreted as follows: instead of simulating decay and diffusion simultaneously through $\hat{\mathrm{H}}$, the signal undergoes pure decay due to Γ followed by pure diffusion due to $D\nabla^2$ in an alternating fashion, repeating over small time steps of order Δt until the desired time t is reached.

We are now in a position to solve the Bloch-Torrey equation efficiently. We begin by discretizing the $3 \times 3 \times 3\,\mathrm{mm}^3$ voxel into N^3 subvoxels. The subvoxels need to be small enough that diffusion effects can be captured during each time step, but large enough that solving the system is still computationally feasible. The root mean square distance

Hamiltonian operator using the method of lines (Schiesser, 1991), wherein space is discretized into a uniform set of grid points r_i, the Laplacian ∇^2 is approximated using second order centred finite differences, and Γ is approximated as a diagonal matrix consisting of the values $\Gamma(\mathbf{r}_\mathrm{i})$. This process represents the Hamiltonian $\hat{\mathrm{H}}$ as a matrix **H**, and the magnetization M(r, t) as a vector **M**(t), where each element $\mathbf{M}_\mathrm{i}$(t) represents M($\mathbf{r}_\mathrm{i}$,t). The Hamiltonian matrix **H** then acts on the transverse magnetization **M** through matrix multiplication. The resulting discretized forms of equations (8) and (9) are

$$\frac{\partial}{\partial t}\mathbf{M}(\mathrm{t}) = -\mathbf{H}\mathbf{M}(t) \tag{16}$$

$$\Rightarrow \mathbf{M}(t) = e^{-\mathbf{H}t}\mathbf{M}(0), \tag{17}$$

where the notation $\mathrm{e}^{-\mathbf{H}\mathrm{t}}$, in this context, represents the matrix exponential of the matrix $-\mathbf{H}$t. In our case, despite having N = 512 and therefore an extremely large $\mathrm{N}^3 \times \mathrm{N}^3$ complex matrix **H**, we need only compute the matrix exponential vector product (also known as the action of the matrix exponential), and not exp (−**H**t) itself, which is in general full despite **H** being sparse (Moler and Van Loan, 2003). Algorithms for computing the action of the matrix exponential are known (Al-Mohy and Higham, 2011; Caliari et al., 2014). We use the algorithm described by Al-Mohy and Higham in (Al-Mohy and Higham, 2011), as well as their MATLAB code *expmv*. A comparison of the signal resulting from Algorithm 1 versus equation (17) and expmv is shown in Fig. 2, revealing that the difference between the approximate and exact solution is less than 0.2%. However, the exact solution with *expmv* is almost two orders of magnitude slower than approximations 10 or 11, making it unsuitable for parameter fitting.

Magnetization Propagation Algorithm

1: Initialize: $\mathrm{M}_0 := i, \Delta t := \mathrm{TE}/30, k := 0$
2: **while** $k\Delta t < \mathrm{TE}$ **do**
3: $\quad \mathrm{M}_{k+\frac{1}{2}} := e^{-\Gamma(\mathbf{r})\Delta t}\,\mathrm{M}_k$
4: $\quad \mathrm{M}_{k+1} := \Phi(\mathbf{r}, \Delta t) * \mathrm{M}_{k+\frac{1}{2}}$
5: $\quad$ **if** $(k+1)\Delta t = \mathrm{TE}/2$ **then**
6: $\quad\quad \mathrm{M}_{k+1} := \overline{\mathrm{M}}_{k+1}$
7: $\quad$ **end if**
8: $\quad k := k + 1$
9: **end while**
10: $S(\mathrm{TE}) := \int \mathrm{M}_k\, d^3\mathbf{r}$

travelled by a freely diffusing particle in n-dimensions is

$$d_{rms} = \sqrt{2nD\Delta t}. \tag{15}$$

If we choose Δt = TE/30 = 2 ms and the diffusion constant $\mathrm{D} = 3.037\ \mu\mathrm{m}^2/\mathrm{ms}$ (Holz et al., 2000), the mean free diffusion distance in n = 3 dimensions is d = 6.04 μm. Choosing N = 512 gives a subvoxel size of 5.86 μm, capturing diffusion effects while being computationally feasible. Algorithm 1 details how to compute the signal at time TE using the approximate evolution equation (10). To assess the accuracy of the approximate solution from Algorithm 1, we compute the solution of equation (8) directly. This can be achieved by first discretizing the

Algorithm 1. Magnetization propagation algorithm used to simulate the signal S(TE) for a given set of free parameters $\mathrm{CA}_{\mathrm{PEAK}}$, BVF, iBVF, and L. All four free parameters are encoded solely in the complex decay rate Γ(**r**); the rest of the algorithm does not depend on them. The notation M_ν is shorthand for M(**r**,νΔt) throughout the algorithm. If the $\mathrm{O}(\Delta t^3)$ order evolution equation (11) were used instead, line 3 should be modified to decay for only a half time step Δt/2, line 4 should perform the Gaussian convolution in-place, and an extra line should be added directly following the convolution which decays for another half time step Δt/2.

We are now able compute a solution to the original problem of fitting

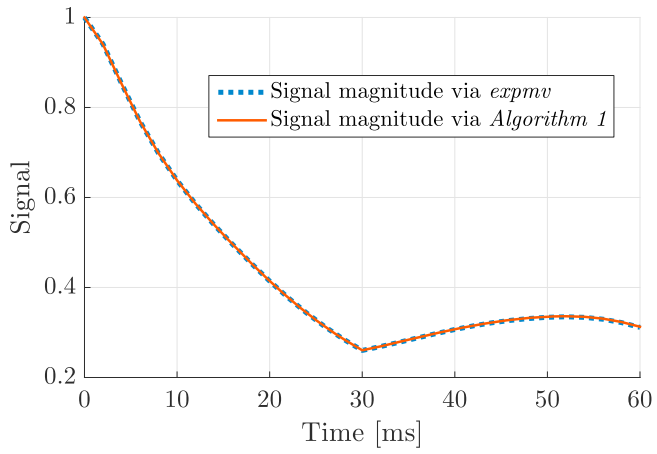

Fig. 2. Comparison between solving the Bloch-Torrey equation exactly using the method of lines in conjunction with Higham's *expmv* integrator (Al-Mohy and Higham, 2011), and solving the Bloch-Torrey equation approximately using the two-step approximate solution as described in Algorithm 1. The signal decay through time calculation shows strong agreement between the two methods, with error values of 0.064% ± 0.045%; the maximum error value of 0.14% occurs at 60 ms.

the simulated ΔR_2 vs. α curve to the observed data on a PC with an Intel Core i7-3930 K CPU and 32 GB of memory running Gnu/Linux within less than a day rather than several weeks. An initial set of simulation parameters (BVF, iRBVF, CA_{PEAK}, and L) are chosen, and the Bloch-Torrey equation (8) is propagated numerically using Algorithm 1 until time TE = 60 ms. ΔR_2 is subsequently calculated for each angle α using equation (1). For L ranging from 1 to 9 the corresponding optimal simulation parameters BVF, iRBVF, and CA_{PEAK} are determined through a gradient descent based non-linear ℓ^2-norm minimization algorithm using MATLAB's *lsqcurvefit* (MATLAB, 2015).

2.3. Experimental procedures

2.3.1. Standard protocol approval, registrations and patient consents

This study was approved by the Clinical Research Ethics Board (Videnskabsetiske Komitéer for Region Midtjylland, M-2013-239-13, August 5th, 2013) and is in accord with the Declaration of Helsinki. All subjects gave written informed consent.

2.3.2. Data acquisition

Data from 10 healthy subjects (3 female; age = 34–65 years, mean = 47.24 years) were acquired on a 3 T system (Skyra, Siemens, Erlangen, Germany). DSC was acquired with spin echo EPI (300 repetitions, TE = 60 ms, TR = 1530 ms, flip angle = 90°, voxel volume = $3 \times 3 \times 3\ mm^3$). 0.2 mmol/kg body weight of Gadovist (Bayer) was injected at a rate of 5 ml/s starting at scan 200, followed by a 30 ml saline flush. Fibre orientation was calculated from a diffusion tensor scan acquired for diffusion kurtosis imaging with a 1 + 3+9 scheme (b-values = 0/1000/2500 s/mm^2, voxel size = $2.29 \times 2.29 \times 2mm^3$, TE = 101 ms, TR = 12200 ms) (Hansen et al., 2013, 2014).

2.3.3. Data processing

Fibre orientation maps were computed from the b = 0 and 2500 s/mm^2 data of the diffusion scan using the approach presented previously (Hernández-Torres et al., 2017). Motion correction, eddy current correction, brain extraction, and computation of the DTI data was performed using FSL's DTIfit (Jenkinson et al., 2012). The DSC data were motion corrected, brain extracted, and registered into DTI space via the fractional anisotropy maps using FSL.

Next, the DSC signal in each WM voxel was sorted into bins according to α, the local angle with respect to the main magnetic field B_0, as determined through the diffusion tensor scan (Hernández-Torres et al., 2015). The voxels of the DSC signal data were split into 18 bins centred around the angles ranging from 2.5° to 87.5° in 5° increments. Each bin was then averaged, resulting in a set of 18 signal vs. time curves parameterized by α. The last step was to calculate ΔR_2 for each curve according to equation (1).

For each voxel, the time point with the lowest T_2-weighted signal was selected as the time point with peak CA concentration. The resulting set of data is a peak ΔR_2 vs. α curve with 18 data points, and it is this set of data that is compared with numerical simulations. In addition, CBF, CBV, and MTT were also calculated as function of fibre orientation, as described previously for gradient echo DSC (Hernández-Torres et al., 2017).

The perfusion parameters CBF, CBV, and MTT were estimated using a parametric approach informed by a physiological model of the microvasculature (Mouridsen et al., 2006, 2014). In this approach, it is assumed that the intravascular contrast agent reaches the capillary bed at a particular blood concentration C(t) modulated by the constant κ, which depends on hematocrit but is assumed constant here. The contrast agent concentration and CBF are then related via

$$\kappa C(t) = \mathrm{CBF} \int_0^t C_\alpha(t-\tau) R(\tau) d\tau, \tag{18}$$

where $C_\alpha(t)$ denotes the arterial input function and R(t) the residue function. The transport function h(t), used to estimate the residue function, is parameterized as a gamma distribution

$$h(t;\alpha,\beta) = -\frac{dR}{dt} = \frac{1}{\beta^\alpha \Gamma(\alpha)} t^{\alpha-1} e^{-t/\beta}, \quad \alpha,\beta > 0. \tag{19}$$

In this approach, MTT equates to αβ = CBV/CBF, where CBF is the peak of the estimated residue function.

3. Results

The presence of CA in WM vasculature causes a change in ΔR_2 that depends on local WM fibre orientation measured with diffusion MRI (Fig. 3). In WM perpendicular to the main magnetic field, ΔR_2 is 20% larger than in fibres parallel to the main magnetic field, as shown by the blue curve in Fig. 3, which represents the average across data acquired in the 10 healthy volunteers. Moreover, the simulated ΔR_2 also depends considerably on the simulated vascular architecture. Since the loss of coherence is mediated by diffusion, not only does the total volume of the blood vessel compartments play a role, the vessel sizes do as well. The simulation with L = 3 anisotropic blood vessels with a radius of 107.6 μm

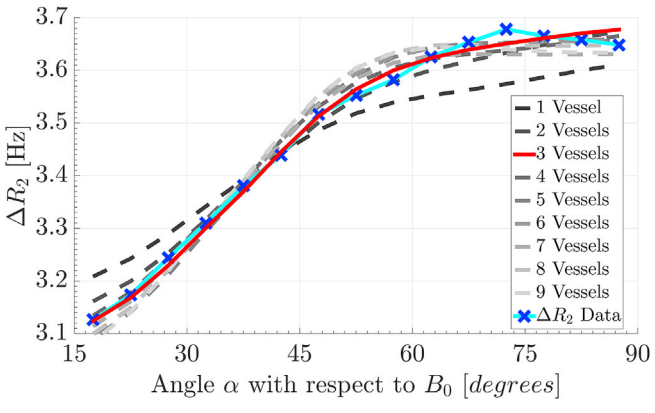

Fig. 3. ΔR_2 versus fibre angle α (blue) and fitted model (red) for L = 3 anisotropic blood vessels. ΔR_2 was 20% larger for fibres perpendicular to the main magnetic field compared to parallel fibres. The resulting parameters found are CA_{PEAK} = 4.00 mM, BVF = 2.82%, and iRBVF = 56.0%, corresponding to a 1.58% isotropic BVF, and a 1.24% anisotropic BVF.

is highlighted in red, as it provided the lowest average error compared to the observed data.

The simulated and measured curves represent a combination of an isotropic vascular component, which results in a constant offset, and an anisotropic component, which results in the observed orientation dependence. Simulations containing only an isotropic vascular bed exhibit no angle dependence, whereas simulations containing only anisotropic vasculature exhibits no offset (not shown), which is in agreement with our earlier findings for gradient echo DSC (Hernández-Torres et al., 2017).

The best fit resulted from $L = 3$ anisotropic vessels with a peak contrast agent concentration of $CA_{PEAK} = 4.00$ mM and a total blood volume fraction of BVF = 2.82%, where iRBVF = 56.0% of the blood is contained in the isotropic vasculature and aRBVF = 44.0% of the blood is contained in the anisotropic vasculature. The radii of the anisotropic vessels range from 52.1 μm for 9 vessels to 206.3 μm for 1 vessel. The best fit corresponds to a vessel radius of 107.6 μm, with the next best fits occurring for $L = 4$ followed by $L = 2$ vessels with radii of 80.3 μm and 137.3 μm, respectively.

It should be noted that more than 97% of data points have an angle with B_0 greater than 15°. For angles below 15°, there was an upward trend that may be an artifact of the small number of voxels contributing to these angles. This trend was not observed in the gradient echo EPI experiment (Hernández-Torres et al., 2017), nor in the simulations of this study, and therefore these points were excluded for the purposes of parameter fitting.

The orientation dependence in ΔR_2 translates to corresponding orientation dependencies in the measured CBF, CBV, and MTT, as shown in Fig. 4. Both CBV and CBF are about 20% larger in WM perpendicular to the main magnetic field compared to WM parallel to the main magnetic field, whereas the temporal parameter MTT shows only a small angle dependence.

4. Discussion

4.1. Solution of the Bloch-Torrey equation

We hypothesized that the vascular anisotropy of WM leads to an orientation dependence of spin echo DSC. We demonstrated this effect experimentally and we presented a rapid approach for parameter fitting that allows us to derive vascular parameters from the orientation dependent DSC signal. For solving the Bloch-Torrey equation (Eq. (8)), we introduced an algorithm which is based on techniques originally developed for quantum mechanics. This algorithm approximates the Green's function of the Bloch-Torrey equation - which cannot be expressed analytically - over small time steps Δt. These intermediate solutions are iteratively updated during each time step until the desired time TE is reached. This method results in solutions that are within a fraction of a percent of the solution computed directly through matrix exponential methods, as illustrated by Fig. 2. Importantly, the solution found by this algorithm is typically one to two orders of magnitude faster to compute for typical simulation parameters than traditional approaches. This is a large advantage over the direct method, as this approach allows us to rapidly investigate varying complex 3D geometries and move quickly through the parameter space. In particular, the minimization to produce Fig. 2 could be performed on a personal computer within a day, rather than weeks.

While the identification between the Bloch-Torrey equation and the imaginary-time Schrödinger equation has been known, methods used to solve the Bloch-Torrey equation that take advantage of quantum-inspired

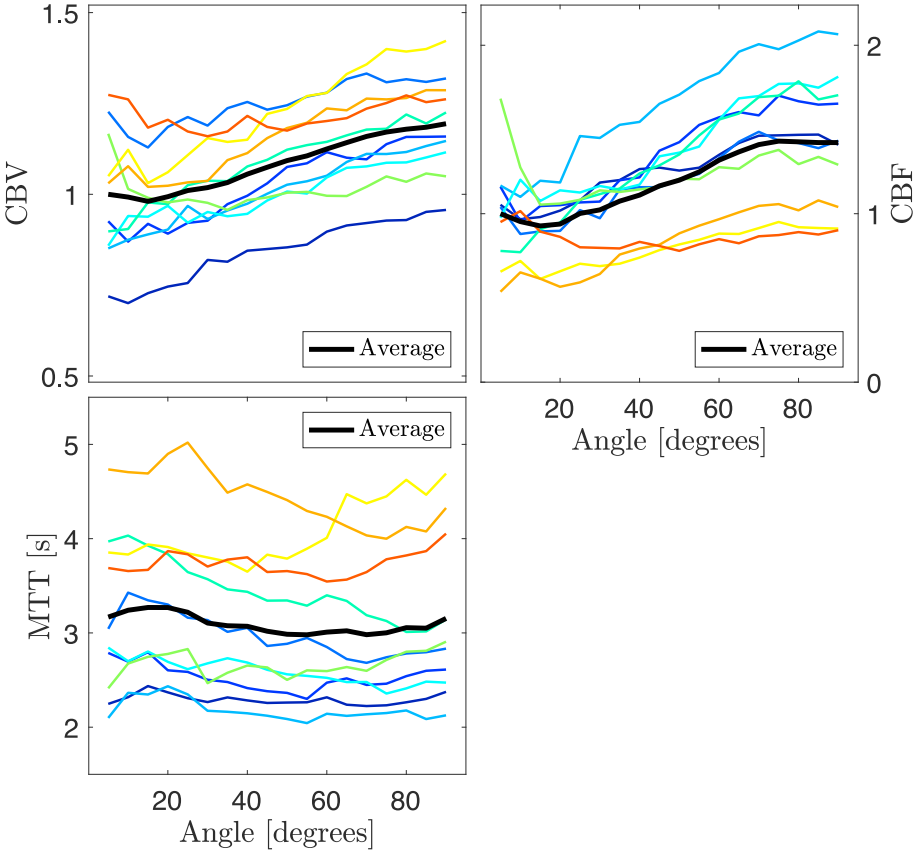

Fig. 4. CBV, CBF, and MTT versus fibre angle α. CBV and CBF exhibit larger values at 90° compared to 0°. The orientation dependence of MTT is weak. Coloured curves represent individual subjects. As no normalization of CBV and CBF to an internal reference tissue was performed, both CBV and CBF are given in arbitrary units, which were normalized to the average from zero to five degrees.

techniques typically use eigenfunction expansion based approaches (Grebenkov, 2008), which are appropriate for quantum mechanical systems. However, these techniques are not useful for large 3D simulations of magnetized spins. As the eigenfunction decomposition is expensive, speed is largely completely sacrificed to begin with. Moreover, the goal of solving the Schrödinger equation in physical systems generally revolves around computing the ground state and the ground state energy, and possibly a small number of excited states above that. In our case, however, we are interested in propagating an initial state through time. Such an approach would require a suitably large eigenbasis in order to represent the magnetization accurately, and this would be prohibitively expensive both to store in memory and to compute.

For these reasons, the Bloch-Torrey equation has most commonly been solved using finite element based (Nguyen et al., 2014) or finite difference based techniques. Such approaches are feasible if only one solution is computed, for example the BOLD effect for a particular vascular geometry, especially when said geometry is given in terms of a realistic vasculature mesh. However, as with matrix exponential based methods, these approaches are too slow and expensive for our problem of iterating through parameter space with the goal of determining the vascular geometry associated with an experimental DSC signal; we need to be able to quickly generate vascular geometries programmatically based on the parameters BVF and iRBVF. Using the splitting method described in Algorithm 1 provides a balance between accuracy and speed in solving the Bloch-Torrey equation.

4.2. Perfusion experiment

We found that the apparent perfusion parameters measured with spin echo DSC imaging depend on the WM fibre orientation, with ΔR_2, CBF, and CBV increasing for increasing angles between WM and the main magnetic field, while the effect was rather small for MTT. The most likely explanation for this phenomenon that is consistent with current scientific knowledge is that a proportion of the vascular network in WM runs in parallel with the fibre tracts. Solving the Bloch-Torrey equation for a range of vascular architectures and CA concentrations and fitting the results to the DSC signal reveals that about half of the WM blood volume is in vessels that run in parallel with the fibre tracts, giving rise to orientation dependent field inhomogeneities.

The finding that 44.0% of the blood resides within anisotropic vasculature and 56.0% in the isotropic component is in good agreement with our earlier gradient echo experiment (Hernández-Torres et al., 2017) in a different cohort. Simulations based on a larger isotropic vessel radius of 13.7 μm obtained with MRI (Jochimsen et al., 2010), which was used in our previous gradient echo study, result in a total blood volume fraction of 3.5%, an anisotropic blood volume fraction of about 34%, and an optimal $L = 5$ large vessels with radii of 81.5 μm. An explanation for the larger total blood volume is that the spin echo experiment is less sensitive to larger vessels (Boxerman et al., 1995). Larger vessels create field inhomogeneities with lower spatial frequencies, causing diffusion to happen within a locally more homogeneous environment. In other words, the spin echo experiment is sensitive to the size of the vessels, in addition to blood volume. Nevertheless, in our simulations the simulated radii of the anisotropic vessels are relatively insensitive to the assumed radii of the isotropic vessels. In gradient echo DSC most of the signal loss is due to static dephasing where the size of the vessels plays no role (Yablonskiy and Haacke, 1994), as long as it is much smaller than the voxel. In our previous gradient echo DSC study, the anisotropic blood volume fraction was, therefore, assumed to be contained in only one anisotropic vessel, even though the same amount of blood volume could reside within more than one vessel. The present study is an extension in that it also provides an estimate of the anisotropic vessel radius. Of course, it is a simplification to assume that all vessels have the same radius. Rather, these vessels with a radius of 107.6 μm should be seen as representative of a number of vessels each with different radii and with orientations that only on average (within a given voxel) are in parallel with the WM tracts. It should also be noted that due to the pooling of voxels from various brain regions, our results are an average for WM across the entire brain. Regional variations in vascular architecture are not addressed by this approach. This, however, does not limit our general experimental observation that the DSC signal depends on local WM fibre orientation. Furthermore, due to partial volume effects such as crossing fibres, local tissue orientation is not equally well defined across all voxels that are pooled together for a certain fibre orientation.

Both an isotropic and an anisotropic vascular component are necessary to explain the observed changes in ΔR_2 of WM. The isotropic component results in a constant offset, whereas the anisotropic component gives rise to the orientation dependence. This finding is equivalent to our previous results for gradient echo DSC (Hernández-Torres et al., 2017), where we showed that the orientation effect in CBF and CBV is about 100%. As expected, the orientation effect is weaker in spin echo DSC than in gradient echo DSC. This observation may also explain why whole brain histograms of CBF are broader for gradient echo DSC than for spin echo DSC, and why arterial spin labelling derived CBF agrees better with spin echo DSC than with gradient echo DSC (Wong et al., 2014).

The best fit resulted in a total blood volume fraction of 2.82%, which is close to the 2.6 ml/100 g for WM tissue determined with positron emission tomography, which is considered the gold standard for CBV measurement (Leenders et al., 1990). A spin echo DSC study reported 1.3 ml/100 g for WM tissue and 4.6 ml/100 g for GM tissue, which converts approximately to 1.3% and 4.6% (Helenius et al., 2003). Using gradient echo DSC, Arakawa et al. reported a CBV of 1.44 ml/100 g in normal appearing WM and 1.86 ml/100 g in normal appearing GM of subjects with stroke (Arakawa et al., 2006). While the CBF determined herein is in good agreement with the PET gold standard, it should be kept in mind that the present study had a relatively small sample size.

The parameter maps CBF and CBV derived from ΔR_2 also show an angle dependence of about 20%, whereas the angle dependence of MTT is small. This finding is in agreement with previous work in gradient echo DSC (Hernández-Torres et al., 2017) and the notion that tissue orientation has an influence on the magnitude of the measured signal but should not have a major influence on the temporal features of the CA bolus measurement.

4.3. Implications for DSC, vessel size imaging, and BOLD fMRI

The vascular anisotropy may have a range of implications for methods that rely on vascular contrast, such as DSC studies, vessel size imaging, and BOLD fMRI. Since the signal to noise ratio of arterial spin labelling is too low in WM, DSC is currently the method of choice for the evaluation of WM perfusion. In multiple sclerosis (Lapointe et al., 2018), for instance, white matter lesions are often seen around central veins (Sati et al., 2016). Therefore, multiple sclerosis lesions that are traversed by a vein parallel to the orientation of the main magnetic field, such as Dawson fingers, may appear to have lower CBF and CBV than lesions around a vein oriented perpendicular to the main magnetic field. Furthermore, the comparison of lesions and contralateral non-lesional tissue needs to control for the presence or absence, and orientation of venous vessels. On the other hand, the orientation dependent approach may allow for more accurate assessment of average perfusion parameters across the whole WM.

A possible orientation effect in DSC can be also seen in Fig. 1 of a publication on WM perfusion in neuropsychiatric lupus by (Papadaki et al., 2018) where CBF is much lower in fibres parallel to the main magnetic field compared to perpendicular fibres.

Vessel size imaging which relies on susceptibility-induced contrast to estimate the CBV and vessel size index (VSI) may also be affected by the orientation dependency of ΔR_2 and ΔR_2^*. Tropès et al. have shown that CBV and VSI derived from ΔR_2 and ΔR_2^* DSC measurements are proportional to ΔR_2^* and $\left(\Delta R_2^*/\Delta R_2\right)^{3/2}$ respectively (Troprès et al., 2001).

Assuming a 20% orientation dependency in ΔR_2 as demonstrated in this work and a 100% dependency in ΔR_2^* as demonstrated in our previous work (Hernández-Torres et al., 2017), one would expect approximately a 100% increase in CBV measured in perpendicular fibres compared to parallel fibres, and a corresponding 115% increase in VSI measurements.

DSC and BOLD fMRI are based on the same physical principles. In BOLD fMRI, an increase in blood oxygenation reduces the magnetic susceptibility difference between veins and surrounding tissue, resulting in a signal increase. Therefore, in BOLD fMRI of the WM (Courtemanche et al., 2018; Ding et al., 2013, 2018; Fabri et al., 2011; Gawryluk et al., 2011; Mazerolle et al., 2013; McWhinney et al., 2012), the vascular anisotropy should lead to tissue angle dependency of the BOLD contrast comparable to that of DSC. The BOLD sensitivity in tracts perpendicular to B_0 may be much larger than the sensitivity in tracts parallel to B_0. Such tissue orientation effect has been reported previously for fMRI of the cortical gray matter (Gagnon et al., 2015). In cortical folds parallel to the main magnetic field, the BOLD signal was shown to be 40% higher compared to folds perpendicular to the main magnetic field. The present work on spin echo DSC and our previous work on gradient echo DSC suggest that the spin echo BOLD signal of WM is less affected (about 20%) than the gradient echo BOLD signal (about 100%).

4.4. Limitations

For the simulation, several simplifications were made. The large vessels were assumed to have the same radius and to run in parallel. Furthermore, the simulated vascular tree is an accumulation of cylinders that are not connected and have no bifurcations. We also ignored that, particularly in WM, the diffusion is anisotropic (Beaulieu and Allen, 1994). However, diffusion along the direction of a vessel does not lead to loss of coherence within that particular vessel's magnetic field. Moreover, we observed that low diffusion coefficients lead to large blood volumes of 5–7% and high CA concentrations, as expected. We therefore assumed a diffusivity equal to that of free water at body temperature for the simulation. One reason why this assumption leads to realistic results may be that arteries, arterioles, veins and venules are surrounded by perivascular spaces, which are filled with cerebrospinal (arterial vessels) and interstitial (venous vessels) fluid. These spaces are approximately two to three times the vessel size and are often enlarged in pathological conditions and normal aging (Doubal et al., 2010; Mestre et al., 2017). The diffusion constant within the fluid-filled perivascular space would be approximately that of water, and since most of the orientation-dependent signal in our model occurs near the anisotropic vessels and therefore within the perivascular space, the approximation of a diffusion constant of water throughout the voxel is not as limiting as it would initially appear. The notion that the fluid within the perivascular spaces can not be neglected is in agreement with very recent work that demonstrates that free water in perivascular spaces significantly affects DTI measures (Sepehrband et al., 2018).

In an effort to support this claim we performed two simulations using a non-constant diffusion coefficient within the voxel, setting the value in the tissue to 2 μm^2/ms and 1.5 μm^2/ms, and solving the Bloch-Torrey equation via equation (17) and the MATLAB code *expmv* by Al-Mohy and Higham. What resulted was an increase in isotropic BVF due to less loss of coherence due to diffusion in the tissue near smaller vessels, but the radius of the anisotropic vessels and the anisotropic BVF remained consistent. We concluded from this that the assumption of a diffusion constant of water throughout the voxel leads only to a minor reduction in isotropic BVF, as expected. It should be noted that despite using a heavily optimized combination of MATLAB and C/C++ code, curve fitting using *expmv* still took over two weeks to complete.

We also ignored that the vessels themselves represent boundaries to the diffusion, since the vessels comprise only a few percent of the tissue. Moreover, there is some inherent T_2' weighting in spin echo EPI that arises from the samples acquired before and after the nominal TE. As these T_2' effects were shown to be small (Duong et al., 2003), they were not taken into account in the present study. That our simulation yielded realistic results for blood volume and CA concentration also suggests that these T_2' effects can be ignored. We also assumed that in our cohort of healthy subjects, there is no extravasation of CA. Moreover, we ignored that prior to the spin echo study and within the same MRI session, subjects also underwent a gradient echo DSC experiment with the administration of 0.1 mmol/kg of the same contrast agent. The minimum delay between the two injections was 7.5 min, allowing for baseline stabilization prior to the second bolus injection. The second ΔR_2 curve was, thus, assumed to be unaffected by the preceding experiment, though some drop in baseline MR signal intensity might be expected.

Due to the design of the study from which our data was obtained, fibre orientation was not measured using conventional DTI but by taking the $b = 0$ and $b = 2500$ scans of a diffusion kurtosis imaging sequence. However, this is unlikely to affect the results, as only the primary eigenvector from the diffusion tensor estimate had to be used for the experiment.

Myelin also gives rise to an orientation dependent signal decay (Denk et al., 2011; Lee et al., 2012; Wharton and Bowtell, 2012). A full 3D model that includes blood vessels, myelinated axons, and possibly ferritin would span several orders of magnitudes of length scales, making it computationally very expensive. Since the orientation-effect of myelin is small compared to the effects due to the contrast agent and also time-independent, myelin was therefore neglected in the current study.

It should be kept in mind that our results are for average WM. Almost certainly, there are brain regions with vascular anisotropy or blood volume that are different from this average, or where the direction of the anisotropic vessels deviates from the WM orientation.

In summary, we show that the spin echo DSC experiment exhibits a strong dependence on the angle between WM tissue and the main magnetic field. In addition, we present a rapid Bloch-Torrey solution, which allows us to derive tissue parameters by fitting a model to the measured data. We show that half of the blood resides in an isotropic vascular network, and half in vessels that run, on average, in parallel with WM tissue.

Author contributions

JD: data analysis, numerical simulations, interpretation of results, writing of manuscript.

LW: numerical simulations.

EHT: data analysis; CK: numerical simulations.

NDF: interpretation of results.

RA, TEL, and BH: data acquisition and interpretation of results.

AR: idea, study supervision, interpretation of results, writing of manuscript all authors contributed to the editing of the manuscript.

Acknowledgements and funding

This work was funded by the Natural Sciences and Engineering Research Council of Canada (016-05371) of Canada and the National Multiple Sclerosis Society (RG-1507-05301). AR is funded by Canada Research Chairs. JD was funded by the Natural Sciences and Engineering Research Council, Canada (USRA - 497681 - 2016). Data and Code Availability: All raw data and code are available from the authors upon request. The framework for the solution of the Bloch-Torrey equation will be made available on our website.

References

Al-Mohy, A., Higham, N., 2011. Computing the action of the matrix exponential, with an application to exponential integrators. SIAM J. Sci. Comput. 33, 488–511. https://doi.org/10.1137/100788860.

Arakawa, S., Wright, P.M., Koga, M., Phan, T.G., Reutens, D.C., Lim, I., Gunawan, M.R., Ma, H., Perera, N., Ly, J., Zavala, J., Fitt, G., Donnan, G.A., 2006. Ischemic thresholds for gray and white matter. Stroke 37, 1211–1216. https://doi.org/10.1161/01.STR.0000217258.63925.6b.

Bader, P., Blanes, S., Casas, F., 2013. Solving the Schrödinger eigenvalue problem by the imaginary time propagation technique using splitting methods with complex coefficients. J. Chem. Phys. 139, 124117. https://doi.org/10.1063/1.4821126.

Beaulieu, C., Allen, P.S., 1994. Determinants of anisotropic water diffusion in nerves. Magn. Reson. Med. Off. J. Soc. Magn. Reson. Med. Soc. Magn. Reson. Med. 31, 394–400.

Bouma, G.J., Muizelaar, J.P., 1990. Relationship between cardiac output and cerebral blood flow in patients with intact and with impaired autoregulation. J. Neurosurg. 73, 368–374. https://doi.org/10.3171/jns.1990.73.3.0368.

Boxerman, J.L., Hamberg, L.M., Rosen, B.R., Weisskoff, R.M., 1995. MR contrast due to intravascular magnetic susceptibility perturbations. Magn. Reson. Med. 34, 555–566.

Cai, K., Tain, R., Das, S., Damen, F.C., Sui, Y., Valyi-Nagy, T., Elliott, M.A., Zhou, X.J., 2015. The feasibility of quantitative MRI of perivascular spaces at 7T. J. Neurosci. Meth. 256, 151–156. https://doi.org/10.1016/j.jneumeth.2015.09.001.

Caliari, M., Kandolf, P., Ostermann, A., Rainer, S., 2014. Comparison of software for computing the action of the matrix exponential. BIT Numer. Math. 54, 113–128. https://doi.org/10.1007/s10543-013-0446-0.

Cavaglia, M., Dombrowski, S.M., Drazba, J., Vasanji, A., Bokesch, P.M., Janigro, D., 2001. Regional variation in brain capillary density and vascular response to ischemia. Brain Res. 910, 81–93. https://doi.org/11489257.

Courtemanche, M.J., Sparrey, C.J., Song, X., MacKay, A., D'Arcy, R.C.N., 2018. Detecting white matter activity using conventional 3 Tesla fMRI: an evaluation of standard field strength and hemodynamic response function. Neuroimage 169, 145–150. https://doi.org/10.1016/j.neuroimage.2017.12.008.

Deistung, A., Rauscher, A., Sedlacik, J., Stadler, J., Witoszynskyj, S., Reichenbach, J.R., 2008. Susceptibility weighted imaging at ultra high magnetic field strengths: theoretical considerations and experimental results. Magn. Reson. Med. 60, 1155–1168. https://doi.org/10.1002/mrm.21754.

Denk, C., Hernández Torres, E., MacKay, A., Rauscher, A., 2011. The influence of white matter fibre orientation on MR signal phase and decay. NMR Biomed. 24, 246–252. https://doi.org/10.1002/nbm.1581.

Denk, C., Rauscher, A., 2010. Susceptibility weighted imaging with multiple echoes. J. Magn. Reson. Imaging JMRI 31, 185–191. https://doi.org/10.1002/jmri.21995.

Ding, Z., Huang, Y., Bailey, S.K., Gao, Y., Cutting, L.E., Rogers, B.P., Newton, A.T., Gore, J.C., 2018. Detection of synchronous brain activity in white matter tracts at rest and under functional loading. Proc. Natl. Acad. Sci. U. S. A 115, 595–600. https://doi.org/10.1073/pnas.1711567115.

Ding, Z., Newton, A.T., Xu, R., Anderson, A.W., Morgan, V.L., Gore, J.C., 2013. Spatio-temporal correlation tensors reveal functional structure in human brain. PloS One 8, e82107. https://doi.org/10.1371/journal.pone.0082107.

Doubal, F.N., MacLullich, A.M.J., Ferguson, K.J., Dennis, M.S., Wardlaw, J.M., 2010. Enlarged perivascular spaces on MRI are a feature of cerebral small vessel disease. Stroke 41, 450–454. https://doi.org/10.1161/STROKEAHA.109.564914.

Duong, T.Q., Yacoub, E., Adriany, G., Hu, X., Ugurbil, K., Kim, S.-G., 2003. Microvascular BOLD contribution at 4 and 7 T in the human brain: gradient-echo and spin-echo fMRI with suppression of blood effects. Magn. Reson. Med. 49, 1019–1027. https://doi.org/10.1002/mrm.10472.

Fabri, M., Polonara, G., Mascioli, G., Salvolini, U., Manzoni, T., 2011. Topographical organization of human corpus callosum: an fMRI mapping study. Brain Res. 1370, 99–111. https://doi.org/10.1016/j.brainres.2010.11.039.

Gagnon, L., Sakadžić, S., Lesage, F., Musacchia, J.J., Lefebvre, J., Fang, Q., Yücel, M.A., Evans, K.C., Mandeville, E.T., Cohen-Adad, J., Polimeni, J.R., Yaseen, M.A., Lo, E.H., Greve, D.N., Buxton, R.B., Dale, A.M., Devor, A., Boas, D.A., 2015. Quantifying the microvascular origin of BOLD-fMRI from first principles with two-photon microscopy and an oxygen-sensitive nanoprobe. J. Neurosci. Off. J. Soc. Neurosci. 35, 3663–3675. https://doi.org/10.1523/JNEUROSCI.3555-14.2015.

Gawryluk, J.R., D'Arcy, R.C.N., Mazerolle, E.L., Brewer, K.D., Beyea, S.D., 2011. Functional mapping in the corpus callosum: a 4T fMRI study of white matter. Neuroimage 54, 10–15. https://doi.org/10.1016/j.neuroimage.2010.07.028.

Grebenkov, D.S., 2008. Laplacian eigenfunctions in NMR. I. A numerical tool. Concepts Magn. Reson. 32A, 277–301. https://doi.org/10.1002/cmr.a.20117.

Guardiola, R., 1998. Monte Carlo methods in quantum many-body theories. Microscopic Quantum Many-Body Theories and Their Applications, Lecture Notes in Physics. Springer, Berlin, Heidelberg, pp. 269–336. https://doi.org/10.1007/BFb0104529.

Hansen, B., Lund, T.E., Sangill, R., Jespersen, S.N., 2013. Experimentally and computationally fast method for estimation of a mean kurtosis. Magn. Reson. Med. 69, 1754–1760. https://doi.org/10.1002/mrm.24743.

Hansen, B., Lund, T., Sangill, R., Jespersen, S., 2014. Erratum: Hansen, Lund, Sangill, and Jespersen. Experimentally and computationally fast method for estimation of a mean kurtosis. Magnetic Resonance in Medicine 69:1754–1760 (2013). Magn. Reson. Med. 71 https://doi.org/10.1002/mrm.25090, 2250–2250.

Helenius, J., Perkiö, J., Soinne, L., Østergaard, L., Carano, R. a. D., Salonen, O., Savolainen, S., Kaste, M., Aronen, H.J., Tatlisumak, T., 2003. Cerebral hemodynamics in a healthy population measured by dynamic susceptibility contrast MR imaging. Acta Radiol. Stockh. Swed. 44, 538–546, 1987.

Hernández-Torres, E., Kassner, N., Forkert, N.D., Wei, L., Wiggermann, V., Daemen, M., Machan, L., Traboulsee, A., Li, D., Rauscher, A., 2017. Anisotropic cerebral vascular architecture causes orientation dependency in cerebral blood flow and volume measured with dynamic susceptibility contrast magnetic resonance imaging. J. Cereb. Blood Flow Metab. Off. J. Int. Soc. Cereb. Blood Flow Metab. 37, 1108–1119. https://doi.org/10.1177/0271678X16653134.

Hernández-Torres, E., Wiggermann, V., Hametner, S., Baumeister, T.R., Sadovnick, A.D., Zhao, Y., Machan, L., Li, D.K.B., Traboulsee, A., Rauscher, A., 2015. Orientation dependent MR signal decay differentiates between people with MS, their asymptomatic siblings and unrelated healthy controls. PloS One 10, e0140956. https://doi.org/10.1371/journal.pone.0140956.

Holz, M., Heil, S.R., Sacco, A., 2000. Temperature-dependent self-diffusion coefficients of water and six selected molecular liquids for calibration in accurate 1H NMR PFG measurements. Phys. Chem. Chem. Phys. 2, 4740–4742. https://doi.org/10.1039/B005319H.

Jenkinson, M., Beckmann, C.F., Behrens, T.E.J., Woolrich, M.W., Smith, S.M., 2012. FSL. NeuroImage 62, 782–790. https://doi.org/10.1016/j.neuroimage.2011.09.015.

Jochimsen, T.H., Ivanov, D., Ott, D.V.M., Heinke, W., Turner, R., Möller, H.E., Reichenbach, J.R., 2010. Whole-brain mapping of venous vessel size in humans using the hypercapnia-induced BOLD effect. Neuroimage 51, 765–774. https://doi.org/10.1016/j.neuroimage.2010.02.037.

Kwee, R., Kwee, T., 2007. Virchow-Robin spaces at MR imaging. Radiographics 27, 1071–1086.

Lapointe, E., Li, D.K.B., Traboulsee, A.L., Rauscher, A., 2018. What have we learned from perfusion MRI in multiple sclerosis? AJNR Am. J. Neuroradiol. 39, 994–1000. https://doi.org/10.3174/ajnr.A5504.

Lee, J., Shmueli, K., Kang, B.-T., Yao, B., Fukunaga, M., van Gelderen, P., Palumbo, S., Bosetti, F., Silva, A.C., Duyn, J.H., 2012. The contribution of myelin to magnetic susceptibility-weighted contrasts in high-field MRI of the brain. Neuroimage 59, 3967–3975. https://doi.org/10.1016/j.neuroimage.2011.10.076.

Leenders, K.L., Perani, D., Lammertsma, A.A., Heather, J.D., Buckingham, P., Healy, M.J., Gibbs, J.M., Wise, R.J., Hatazawa, J., Herold, S., 1990. Cerebral blood flow, blood volume and oxygen utilization. Normal values and effect of age. Brain J. Neurol. 113 (Pt 1), 27–47.

Marques, J.P., Bowtell, R.W., 2008. Using forward calculations of the magnetic field perturbation due to a realistic vascular model to explore the BOLD effect. NMR Biomed. 21, 553–565. https://doi.org/10.1002/nbm.1224.

Mazerolle, E.L., Gawryluk, J.R., Dillen, K.N.H., Patterson, S.A., Feindel, K.W., Beyea, S.D., Stevens, M.T.R., Newman, A.J., Schmidt, M.H., D'Arcy, R.C.N., 2013. Sensitivity to white matter FMRI activation increases with field strength. PloS One 8, e58130. https://doi.org/10.1371/journal.pone.0058130.

McWhinney, S.R., Mazerolle, E.L., Gawryluk, J.R., Beyea, S.D., D'Arcy, R.C.N., 2012. Comparing gray and white matter fMRI activation using asymmetric spin echo spiral. J. Neurosci. Methods 209, 351–356. https://doi.org/10.1016/j.jneumeth.2012.06.014.

Meier-Ruge, W., Hunziker, O., Schulz, U., Tobler, H.J., Schweizer, A., 1980. Stereological changes in the capillary network and nerve cells of the aging human brain. Mech. Ageing Dev. 14, 233–243.

Mestre, H., Kostrikov, S., Mehta, R.I., Nedergaard, M., 2017. Perivascular spaces, glymphatic dysfunction, and small vessel disease. Clin. Sci. (Lond.) 131, 2257–2274. https://doi.org/10.1042/CS20160381.

Moler, C., Van Loan, C., 2003. Nineteen dubious ways to compute the exponential of a matrix, twenty-five years later. SIAM Rev. 45, 3–49. https://doi.org/10.1137/S00361445024180.

Mouridsen, K., Friston, K., Hjort, N., Gyldensted, L., Østergaard, L., Kiebel, S., 2006. Bayesian estimation of cerebral perfusion using a physiological model of microvasculature. Neuroimage 33, 570–579. https://doi.org/10.1016/j.neuroimage.2006.06.015.

Mouridsen, K., Hansen, M.B., Østergaard, L., Jespersen, S.N., 2014. Reliable estimation of capillary transit time distributions using DSC-MRI. J. Cereb. Blood Flow Metab. Off. J. Int. Soc. Cereb. Blood Flow Metab. 34, 1511–1521. https://doi.org/10.1038/jcbfm.2014.111.

Nguyen, D.V., Li, J.-R., Grebenkov, D., Le Bihan, D., 2014. A finite elements method to solve the Bloch–Torrey equation applied to diffusion magnetic resonance imaging. J. Comput. Phys. 263, 283–302. https://doi.org/10.1016/j.jcp.2014.01.009.

Nonaka, H., Akima, M., Hatori, T., Nagayama, T., Zhang, Z., Ihara, F., 2003a. The microvasculature of the cerebral white matter: arteries of the subcortical white matter. J. Neuropathol. Exp. Neurol. 62, 154–161.

Nonaka, H., Akima, M., Hatori, T., Nagayama, T., Zhang, Z., Ihara, F., 2003b. Microvasculature of the human cerebral white matter: arteries of the deep white matter. Neuropathology 23, 111–118. https://doi.org/10.1046/j.1440-1789.2003.00486.x.

Norris, D.G., 2012. Spin-echo fMRI: the poor relation? Neuroimage 62, 1109–1115. https://doi.org/10.1016/j.neuroimage.2012.01.003.

Ogawa, S., Lee, T.M., Kay, A.R., Tank, D.W., 1990. Brain magnetic resonance imaging with contrast dependent on blood oxygenation. Proc. Natl. Acad. Sci. U. S. A 87, 9868–9872.

Okudera, T., Huang, Y.P., Fukusumi, A., Nakamura, Y., Hatazawa, J., Uemura, K., 1999. Micro-angiographical studies of the medullary venous system of the cerebral hemisphere. Neuropathol. Off. J. Jpn. Soc. Neuropathol. 19, 93–111. https://doi.org/10.1046/j.1440-1789.1999.00215.x.

Østergaard, L., Sorensen, A.G., Kwong, K.K., Weisskoff, R.M., Gyldensted, C., Rosen, B.R., 1996a. High resolution measurement of cerebral blood flow using intravascular tracer bolus passages. Part II: experimental comparison and preliminary results. Magn. Reson. Med. 36, 726–736.

Østergaard, L., Weisskoff, R.M., Chesler, D.A., Gyldensted, C., Rosen, B.R., 1996b. High resolution measurement of cerebral blood flow using intravascular tracer bolus passages. Part I: mathematical approach and statistical analysis. Magn. Reson. Med. 36, 715–725.

Papadaki, E., Fanouriakis, A., Kavroulakis, E., Karageorgou, D., Sidiropoulos, P., Bertsias, G., Simos, P., Boumpas, D.T., 2018. Neuropsychiatric lupus or not? Cerebral hypoperfusion by perfusion-weighted MRI in normal-appearing white matter in primary neuropsychiatric lupus erythematosus. Ann. Rheum. Dis. 77, 441–448. https://doi.org/10.1136/annrheumdis-2017-212285.

Reichenbach, J.R., Haacke, E.M., 2001. High-resolution BOLD venographic imaging: a window into brain function. NMR Biomed. 14, 453–467.

Sati, P., Oh, J., Constable, R.T., Evangelou, N., Guttmann, C.R.G., Henry, R.G., Klawiter, E.C., Mainero, C., Massacesi, L., McFarland, H., Nelson, F., Ontaneda, D., Rauscher, A., Rooney, W.D., Samaraweera, A.P.R., Shinohara, R.T., Sobel, R.A., Solomon, A.J., Treaba, C.A., Wuerfel, J., Zivadinov, R., Sicotte, N.L., Pelletier, D., Reich, D.S., NAIMS Cooperative, 2016. The central vein sign and its clinical evaluation for the diagnosis of multiple sclerosis: a consensus statement from the North American Imaging in Multiple Sclerosis Cooperative. Nat. Rev. Neurol. 12, 714–722. https://doi.org/10.1038/nrneurol.2016.166.

Schiesser, W., 1991. The numerical method of lines - 1st edition [WWW Document]. https://www.elsevier.com/books/the-numerical-method-of-lines/schiesser/978-0-12-624130-3. accessed 5.24.18.

Sepehrband, F., Cabeen, R., Choupan, J., Barisano, G., Law, M., Toga, A., for the Alzheimer's Disease Neuroimaging Initiative, 2018. A Systematic Bias in DTI Findings bioRxiv 395012. https://doi.org/10.1101/395012.

Spijkerman, J., Petersen, E., Hendrikse, J., Luijten, P., Zwanenburg, J., 2018. T2 mapping of cerebrospinal fluid: 3T versus 7T. MAGMA 3, 415–424. https://doi.org/10.1007/s10334-017-0659-3.

Stanisz, G.J., Odrobina, E.E., Pun, J., Escaravage, M., Graham, S.J., Bronskill, M.J., Henkelman, R.M., 2005. T1, T2 relaxation and magnetization transfer in tissue at 3T. Magn. Reson. Med. 54, 507–512.

Torrey, H.C., 1956. Bloch equations with diffusion terms. Phys. Rev. 104, 563–565. https://doi.org/10.1103/PhysRev.104.563.

Troprès, I., Grimault, S., Vaeth, A., Grillon, E., Julien, C., Payen, J.F., Lamalle, L., Décorps, M., 2001. Vessel size imaging. Magn. Reson. Med. 45, 397–408.

Uludağ, K., Blinder, P., 2018. Linking brain vascular physiology to hemodynamic response in ultra-high field MRI. Neuroimage 168, 279–295. https://doi.org/10.1016/j.neuroimage.2017.02.063.

Uludağ, K., Müller-Bierl, B., Uğurbil, K., 2009. An integrative model for neuronal activity-induced signal changes for gradient and spin echo functional imaging. Neuroimage 48, 150–165. https://doi.org/10.1016/j.neuroimage.2009.05.051.

Wharton, S., Bowtell, R., 2012. Fiber orientation-dependent white matter contrast in gradient echo MRI. Proc. Natl. Acad. Sci. U. S. A 109, 18559–18564. https://doi.org/10.1073/pnas.1211075109.

Wick, G.C., 1954. Properties of bethe-salpeter wave functions. Phys. Rev. 96, 1124–1134. https://doi.org/10.1103/PhysRev.96.1124.

Wong, A.M., Yan, F.-X., Liu, H.-L., 2014. Comparison of three-dimensional pseudo-continuous arterial spin labeling perfusion imaging with gradient-echo and spin-echo dynamic susceptibility contrast MRI. J. Magn. Reson. Imaging JMRI 39, 427–433. https://doi.org/10.1002/jmri.24178.

Yablonskiy, D.A., Haacke, E.M., 1994. Theory of NMR signal behavior in magnetically inhomogeneous tissues: the static dephasing regime. Magn. Reson. Med. Off. J. Soc. Magn. Reson. Med. Soc. Magn. Reson. Med. 32, 749–763.

Ziener, C.H., Glutsch, S., Jakob, P.M., Bauer, W.R., 2009. Spin dephasing in the dipole field around capillaries and cells: numerical solution. Phys. Rev. E - Stat. Nonlinear Soft Matter Phys. 80, 046701. https://doi.org/10.1103/PhysRevE.80.046701.

Ziener, C.H., Kampf, T., Melkus, G., Jakob, P.M., Schlemmer, H.-P., Bauer, W.R., 2012. Signal evolution in the local magnetic field of a capillary – analogy to the damped driven harmonic oscillator. Magn. Reson. Imaging 30, 540–553. https://doi.org/10.1016/j.mri.2011.12.006.